Bow shock clustering in particle-laden wetted cylinder flow

Zhaoyu Shi [a], Fengjian Jiang [b,*], Håkon Strandenes [c], Lihao Zhao [d,a], Helge I Andersson [a]

[a] *Department of Energy and Process Engineering, Norwegian University of Science and Technology, 7491 Trondheim, Norway*
[b] *Department of Ships and Ocean Structures, SINTEF Ocean, 7052 Trondheim, Norway*
[c] *Kreuzinger und Manhart Turbulenz GmbH, 7069 Trondheim, Norway*
[d] *AML, Department of Engineering Mechanics, Tsinghua University, 100084 Beijing, China*

ARTICLE INFO

ABSTRACT

The inhomogeneous distributions of inertial particles in the unsteady flow around a wetted circular cylinder at $Re = 100$ were investigated in one-way coupled three-dimensional numerical simulations. The Kármán vortex cells determine the local patterns of particle clustering. In the vicinity of the cylinder, a bow shock-like clustering was explored via Voronoï diagrams. The shape of the bow shock in terms of width and thickness strongly depends on Stokes number, Sk. For high-Sk particles, the bow shock was wider and less affected by the vortex shedding in the near wake and thus extended further downstream. We tracked low-Sk particles in a steady potential flow aimed at mimicking the viscous flow field close to the cylindrical surface. The converging tendency of the particle trajectories at the upstream of the cylinder supported the appearance of a bow shock. Furthermore, we analysed the trajectory of a Sk=0.1 particle in viscous flow, wherein the direction of the perpendicular component of the Stokes drag force was altered from outwards to inwards at the inflection point of the trajectory. This observation suggests that the centrifugal mechanism makes particle trajectories converge and thereby contributes to the formation of the bow shock.

1. Introduction

Inertial particles suspended in fluid flows are commonly encountered in industrial and environmental settings, such as the scouring around near-shore wind turbine foundations, particle deposition and erosion in turbomachines, in combustion systems, and aerosol scavenging around buildings etc. Numerous experimental and numerical studies on particle-laden flows have been conducted in homogeneous isotropic turbulence (HIT) (Ireland et al. 2016; Sumbekova et al. 2017), and channel flows (Fessler et al. 1994; Marchioli and Soldati, 2002; Zhao et al. 2010), but to a lesser extent in wake flows. Pioneering research on a particle-laden wake behind a plane revealed that the large-scale vortical structures lead to distinctly inhomogeneous particle distributions even though the particles were uniformly seeded. A significant feature of this self-organized behaviour is known as particle *clustering*. Tang et al. (1992) simulated particle dispersion in the wake behind a thick plane and made comparisons with a plane mixing layer. It was shown that the evolution of large-scale vortices influenced the spatial clustering patterns. Their findings were subsequently sup-

ported by experimental results from Yang et al. (2000), which confirmed the strong dependency of the clustering on particle inertia, consistent with the numerical simulations by Tang et al. (1992).

Only a few studies focus on particle clustering in flow past a circular cylinder and in the wake behind the cylinder. This lack of investigations contrasts with the substantial focus on single-phase flow around circular cylinders, which has been thoroughly studied over several decades both in laminar and turbulent regimes; see e.g. Williamson (1996) and Zdravkovich (1997). Representative studies employing direct numerical simulations (DNS) by Luo et al. (2009) and a lattice-Boltzmann method (LBM) by Zhou et al. (2011) observed that inertial particles are mostly encountered in high-strain-rate regions at moderate Reynolds numbers. More recent papers by Homann and Bec, 2015 and Vallée et al. 2018 explored particle dispersion in the wake of a sphere, which can be regarded to share qualitative features with the cylinder wake flow. However, most investigations have provided only phenomenological descriptions of the clustering process, without the relevant physical insight in the phenomenon. This contrasts with the studies of particle clustering in HIT, in which alternative mechanisms have been proposed to explain the non-uniform particle distribution. The preferred explanations are the 'centrifugal' mechanism (Maxey 1987; Fessler et al. 1994) applicable for low-

---

inertia particles strongly coupled with the carrier flow at relatively low Reynolds number, and the 'sweep-stick' mechanism suggested by Goto and Vassilicos, 2008 for heavier particles in flows at higher Reynolds number with broad-banded turbulence.

A few different approaches have been applied to quantitatively characterize the particle clustering. The box-counting method, adopted by Fessler et al. (1994), utilizes uniform boxes to measure the probability density function (PDF) and is simple to implement but sensitive to the chosen box size. Another direct method introduced by Melheim (2005) is to define a spherical or elliptical cutoff length of two colliding particles in order to detect particle clusters. Lagrangian statistics, i.e. time correlations (Uhlmann 2008) and radial distribution functions (RDF; Wood et al. 2005), are based on the particle velocity and distance along trajectories to provide the possibility of finding particles. A drawback is that Lagrangian statistics are unable to provide instantaneous particle clustering but only give global information. A relatively new technique, known as Voronoï analysis or tessellation, was introduced by Monchaux and Bourgoin, 2010 and successfully applied to estimate the instantaneous particle clustering in channel flows (Nilsen et al. 2013) and HIT (Tagawa et al. 2012) for both point-like and finite-size particles. An advantage of this diagnostic tool is its efficiency in dealing with numerous particles, e.g. of the order of 10^5. Monchaux et al. (2012) compared other common methods mentioned above and pointed out the challenge of tracking dynamical clusters. Voronoï analysis is likely to be an attractive diagnostic tool in bluff-body wake flows in general and in cylinder wakes in particular.

To realistically model particle dispersion in cylinder wake flows, particle-wall collisions are essential, whereas interparticle collisions are negligible as long as the suspension is sufficiently dilute. In industrial processes, such as filtration and coagulation of aerosols, slurry transport etc., the interstitial viscous fluid is no longer negligible, like in dry granular flow, but instead acts as a resistant or lubrication force which may lead to a certain particle kinetic energy loss. An elastic restitution coefficient may account for the energy loss. Joseph et al. (2001) experimentally studied the normal coefficient of restitution (ratio of the rebound to impact particle velocity), wherein the normal coefficient is close to zero within a certain critical range of particle inertia. This suggests that no rebound of particles appears below the threshold. Kantak and Davis (2004) extended the analysis to the tangential coefficient of restitution under oblique collisions and concluded that the tangential velocity is barely damped with the corresponding restitution coefficient close to unity over a wide range of particle inertia. Therefore, particle motion can be approximately modeled not as rebound but sliding along the wall. Kantak and Davis (2006) also provided comprehensive analytical expressions for the restitution coefficients, which supported the previous experimental results of Kantak and Davis (2004). Cylinders with wetted surfaces occur in two-phase flow reactors in oil refineries, during dip coating processes (Quéré, 1999; Scriven, 1988), and in so-called fog harvesting when liquid films are formed on the collecting wires, see Shi et al. (2018).

The majority of studies on particle-laden cylinder wake flow focus on the dynamic interaction between particles and coherent structures or vortex cells in the wake. There are only a few studies on particle movements in the vicinity of a cylindrical body, which is controlled by the particle-wall collision model. A striking phenomenon, known as a *bow shock*, was observed in front of a cylinder immersed in a dilute dry granular flow, see e.g. Wassgren et al. (2003) and Bharadwaj et al. (2006). They analyzed the dependency of the particle drag force constructed from the restitution coefficient on Mach and Knudsen numbers. Of particular interest is that a bow shock structure was not only formed in a supersonic flow (Boudet et al. 2008) but also in incompress-

ible flows. To the best of our knowledge, a particulate bow shock structure has never been observed in dilute suspensions of inertial particles in continuous incompressible viscous flows.

This paper presents observations of a bow shock in a simulated wet cylinder flow, and quantitatively investigates how particle inertia effects change the shape of the bow shock via Voronoï diagrams. A sliding particle-wall collision model is adopted to mimic a wetted circular cylinder coated by a thin film layer. The details of the mathematical modeling as well as the computational methods and parameters are given in Section 2 of the paper. A discussion of Voronoï data and explanations based on a potential flow approach is given in Section 3. In Section 4, centrifuging is suggested as a mechanism responsible for the observed convergence of particle trajectories, which eventually leads to bow-shock formation. Finally, Section 5 summarizes the important observations and draws the conclusions.

2. Problem description

2.1. Governing equations and numerical methods

We perform three-dimensional numerical simulations by directly solving the transient flow around a circular cylinder at Reynolds number $Re = U_0 D/\nu = 100$ (U_0 is the free-stream velocity, D is cylinder diameter). The well-verified DNS/LES solver MGLET (Manhart et al. 2001; Manhart and Friedrich 2002) utilizes a second-order finite volume method to discretize the mass conservation and Navier-Stokes equation for incompressible flow

$$\frac{\partial u_i}{\partial x_i} = 0, \tag{1}$$

$$\underbrace{\frac{\partial u_i}{\partial t}}_{\text{acceleration}} + \underbrace{u_j \frac{\partial u_i}{\partial x_j}}_{\text{convection}} = \underbrace{-\frac{1}{\rho_f} \frac{\partial p}{\partial x_i}}_{\text{pressure force}} + \underbrace{\nu \frac{\partial^2 u_i}{\partial x_j \partial x_j}}_{\text{viscous diffusion}} . \tag{2}$$

The instantaneous fluid velocity components u_i and pressure p are stored in discrete staggered equidistant three-dimensional Cartesian grids. The solution is advanced in time by an explicit low-storage third-order Runge-Kutta scheme. The Poisson equation is iteratively solved by Stone's strongly implicit procedure (SIP). The cuboid Cartesian cells are intersected by the curved cylinder wall, and the shapes of those polyhedron cells are exactly computed from the intersection by an immersed boundary method (IBM) with cut-cell implementation. The *cut-cell* approach is employed to obtain the precise surface geometry and normal vector of the intersected cells to handle the particle-wall collision boundary condition, whereas the conventional ghost-cell approach in MGLET cannot (Peller et al. 2006).

We consider the movement of inertial point-like spheres ($\rho_p/\rho_f = 1000$, where ρ_p and ρ_f are the densities of the particles and the fluid, respectively). The particle loading is low with a volume fraction below 10^{-6}, such that the flow is unaffected by the presence of the particles and one-way coupling between the particle and fluid phases can be justified wherever the particles are not too densely clustered. The Maxey-Riley equation (Maxey and Riley 1983), which describes the individual particle motion in a Lagrangian framework, is simplified to:

$$\frac{du_{p,i}}{dt} = \frac{C_D Re_p}{24\tau_p}(u_{f@p,i} - u_{p,i}), \tag{3}$$

$$\frac{dx_{p,i}}{dt} = u_{p,i}, \tag{4}$$

where only the Stokes drag force is acting on a particle and all other forces are assumed negligible in Eq. (3). The particle velocity $u_{p,i}$ is updated by an adaptive fourth-order Rosenbrock-Wanner

Table 1
Characteristics of the flow configuration and the corresponding force coefficients.

Flow configuration			Main flow coefficients		
$\Delta x_{min}/D$	Domain size $(L_x/D \times L_y/D \times L_z/D)$	Cell number (million)	C_d	C_{l-rms}	St
0.016	32.768 × 16.384 × 4.096	14.42	1.3932	0.2401	0.1694

scheme with a third-order error estimator (Gobert 2010), while the fluid velocity component $u_{f@p,i}(t) = u(t, x_{p,i}(t))$ seen by the particle at position $x_{p,i}$ is obtained by linear interpolation. The particle position x_p is obtained from the kinematic relation in Eq. (4). An explicit Euler scheme is used to update particle position. The particle relaxation time $\tau_p = \rho_p d^2/18\rho_f \nu$ where d is particle diameter, is used to define the Stokes number $Sk = \tau_p/\tau_f$ as a non-dimensional parameter to measure the particle inertia. Here, $\tau_f = D/U_0$ is a nominal flow time scale. The drag coefficient C_D is taken as a function of particle Reynolds number $Re_p = d \parallel \boldsymbol{u}_p - \boldsymbol{u}_{f@p} \parallel /\nu$ in order to allow for finite-Re_p corrections to the Stokes limit $Re_p \to 0$. We adopt a piecewise model of C_D, covering different ranges of Re_p; see Cliff et al. (1978) and the recent paper by Shi et al. (2019). In practice, however, the Reynolds number Re_p is always lower than 3×10^5 in the present cases, for which the corresponding C_D formula

$$C_D = \frac{24}{Re_p}(1 + 0.15Re_p^{0.687}) + \frac{0.42}{1 + 4.25 \times 10^4 Re_p^{-1.16}} \quad (5)$$

is activated.

2.2. Computational set-up

The Eulerian PDEs (1,2) governing the fluid flow are integrated on a three-dimensional computational domain discretized by a multi-level structured Cartesian mesh, which is constructed by different sizes of grid boxes filled with the same number of grid cells. A local grid refinement is enforced by embedding zonal grids around the cylinder (Manhart 2004). The center of the cylinder is at (X = 0, Y = 0). The inlet boundary condition for all simulations is a constant free-stream velocity $(u, v, w) = (U_0, 0, 0)$ and a Neumann condition $\partial p/\partial x = 0$ on pressure. Zero pressure and Neumann conditions on the three velocity components, i.e. $\partial u/\partial x = \partial v/\partial x = \partial w/\partial x = 0$, are applied at outlet of the domain. Periodicity is imposed at the two vertical side-walls; i.e. normal to the spanwise Z-direction. Free-slip boundary conditions are used in the crossflow Y-direction, i.e. $v = 0$ and $\partial u/\partial y = \partial w/\partial y = 0$. The dimensions of the computational domain are provided in Table 1, which also reports the time-averaged drag coefficient $C_d = 2F_d/\rho_f U_0^2 LD$ (F_d : drag force, L: cylinder length), the standard deviation of the lift coefficient $C_{l-rms} = 2F_{l-rms}/\rho_f U_0^2 LD$ (F_{l-rms} : root-mean-square lift force) and Strouhal number $St = f\tau_f = fD/U_0$ (f : vortex shedding frequency). The present values are close to the reference ranges 1.32 ~ 1.42, 0.22 ~ 0.29 and 0.164 ~ 0.168 in Kim et al. (2001), Su et al. (2007) and Tseng and Ferziger (2003), respectively.

Inertial point-particles are seeded into the flow field with initial velocity $u_p(t_0) = U_0$ at the inlet. The particle seeding started when a strictly periodic vortex shedding had been established at $t_0 = 250\tau_f$. Nine different nominal Stokes numbers Sk are considered. These different particles can be classified, according to their mass, into three categories; see Table 2. Depending on the particle inertia, parameterized by Sk, particles may or may not collide with the cylinder. During collisions between particles and the wet cylinder surface, the energy loss is associated with the wall-normal and wall-tangential velocity components. According to previous conclusion concerning the restitution coefficients (Joseph

**Table 2**
Particle information for different simulations.

Particle class	Light	Medium	Heavy
Sk	1 3 5	8 12 16	24 40 56
Particles per Sk		~ 10^5	

et al. 2001; Kantak and Davis 2006), the normal restitution coefficient is zero at low Stokes numbers while the tangential one is approximately unity. Therefore, we adopt the *sliding motion* collision model as the boundary condition for impacting particles, wherein the ratios of normal and tangential momentum losses are unity and zero, respectively.

3. Bow shock particle clustering

3.1. Density inhomogeneities

It is well-known that the flow past a straight circular cylinder at $Re = 100$ remains two-dimensional and laminar although it becomes unsteady. Fig. 1 presents the snapshots of inertial particle distributions over the whole domain for Sk = 1, 5, 16, 56, superimposed on the instantaneous spanwise vorticity (ω_z), which reflects the typical Kármán vortex street in the wake behind the cylinder. Since the flow is two-dimensional and two-componential, i.e. the two velocity components u and v are independent of Z, all particles can be projected into a single XY-plane to increase the statistical samples. Density inhomogeneities are noticeable both in the near and far wake in Fig. 1. For the low-Sk case shown in Fig. 1(a), particles accumulate locally close to the front of the cylinder as they approach the wall and are therefore convected downstream by the surrounding fluid. Owing to the relatively low Stokes number, the particles tend to follow the carrier flow. These particles are expelled away from the vortex cores and tend to align along the vortex cell boundaries. The higher particle concentration in the front of the cylinder and around the cylinder surface resembles a *bow shock* (more easily seen in Fig. 1(b, c, d)). The shape of the bow shock in the near wake at X ≈ 3D for Sk = 1 is clearly affected by the shed vortices. At higher Stokes numbers, the heavier particles are less coupled to the underlying flow and move almost ballistically towards the cylinder. Therefore, we can observe a clear appearance of a thin particle layer where the darkness reflects the dense particle concentration. This curved high-particle-concentration layer is referred to as *bow shock* in the present study. A similar phenomenon of particle clustering was reported in dilute *granular* flow, see Bharadwaj et al. (2006), in which a wider and thicker bow shock was formed upstream of the cylinder. The present bow shock, however, forms in a fundamentally different flow, namely in a viscous continuum. Moreover, the shock becomes wider for higher Stokes number in Fig. 1(b) ~ (c). We observe, at Sk = 56, that the high-concentration layer extends well into the intermediate wake, i.e. downstream of X ≈ 10D. The various patterns of particle concentration in the near-cylinder region exhibit substantial effects of inertia.
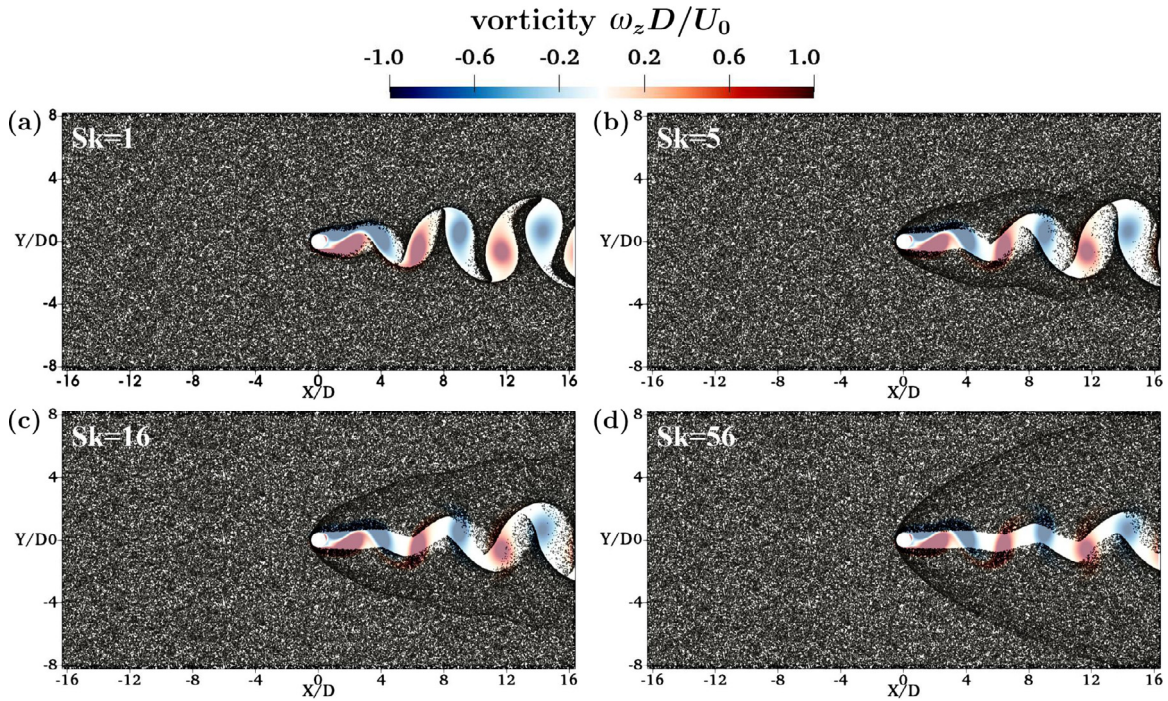
Fig. 1. Instantaneous particle distribution (black dots) projected on an XY-plane. (a)Sk = 1; (b)Sk = 5; (c)Sk = 16; (d)Sk = 56. The background (color) is the spanwise vorticity $\omega_z D/U_0$. (For interpretation of the references to color in this figure legend, the reader is referred to the web version of this article.)
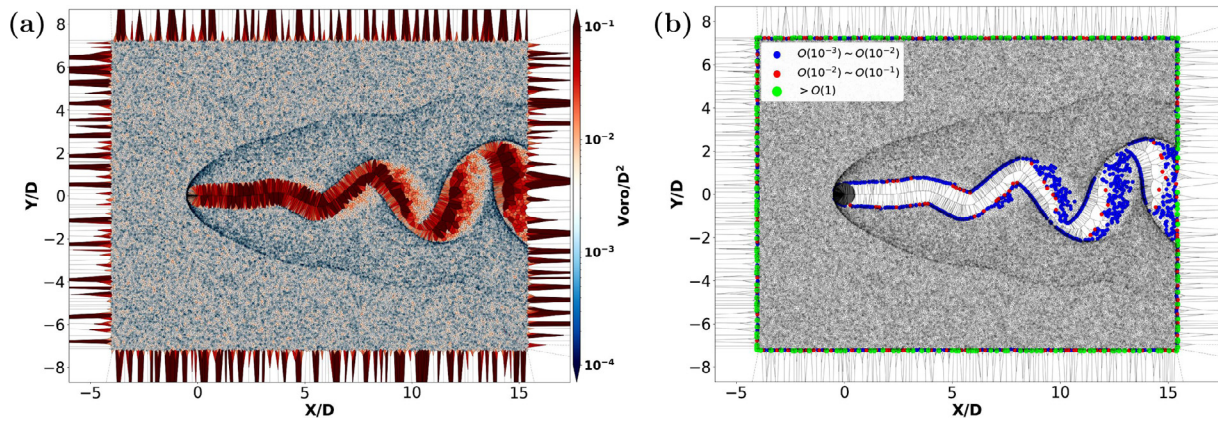

Fig. 2. (a) Example of Voronoï diagrams at Sk = 12. The bow shock (dark dense path) is detected by the smallest Voronoï cells. (b) Abnormal particles with Voronoï area over 1 (green dots) lying along the boundaries of the domain. Particles with Voronoï area between $O(10^{-3})$ and $O(10^{-1})$ (red and blue dots) are located within the vortex structures. (For interpretation of the references to color in this figure legend, the reader is referred to the web version of this article.)

3.2. Voronoï analysis

Voronoï diagrams have been mostly used to quantify particle clustering in HIT and channel flows, but can also be computationally efficient in detecting the bow shock in the cylinder wake. We employed two intrinsic libraries called Voronoï and ConvexHull in Python to calculate the Voronoï cell areas and plot the diagram. Fig. 2(a) shows an example of Voronoï cells in two dimensions at Sk = 12 for illustration, where the domain is divided into polygon cells, each corresponding to one given particle ('site'). All vertices in each Voronoï cell are closer to the site than to any other cell's site. This property, free of any cell-size effects, indicates that the inverse of a Voronoï cell area is a measure of the local particle concentration. The average Voronoï cell area is approximately $O(10^{-3})$ and is given as A_d/N_p, where N_p is the total number of particles and $A_d = L_x \times L_y$ is the area of the two-dimensional plane. The average Voronoï cell area is used only as a reference value and not

for normalization. The bow shock in the vicinity of the cylinder is identified by the substantially smaller Voronoï cell areas of order $O(10^{-6} \sim 10^{-5})$. The Voronoï cells within the vortex cores in the wake are much larger than those identifying the bow shock with areas ranging from $O(10^{-3})$ to $O(10^{-1})$. Thus, inertial particles are rarely observed within the vortex cores. It should be noted that the Voronoï cell areas along the borders of the computational domain are abnormally large. All such ill particles with a cell area value larger than 1 shown in Fig. 2(b) are disregarded in the further post-processing.

A statistical analysis of the Voronoï areas at X = -0.3D, i.e. 0.2D downstream of the stagnation point, is exhibited in Fig. 3. This figure is composed of a scatter plot of the density distribution, a histogram and the kernel density estimation (KDE) curve across the flow. The histogram and KDE plots depicted in Fig. 3 are based on 1.5×10^4 scatter points from an ensemble of 13 different time steps. For each sample point x_i, a Gaussian kernel func-
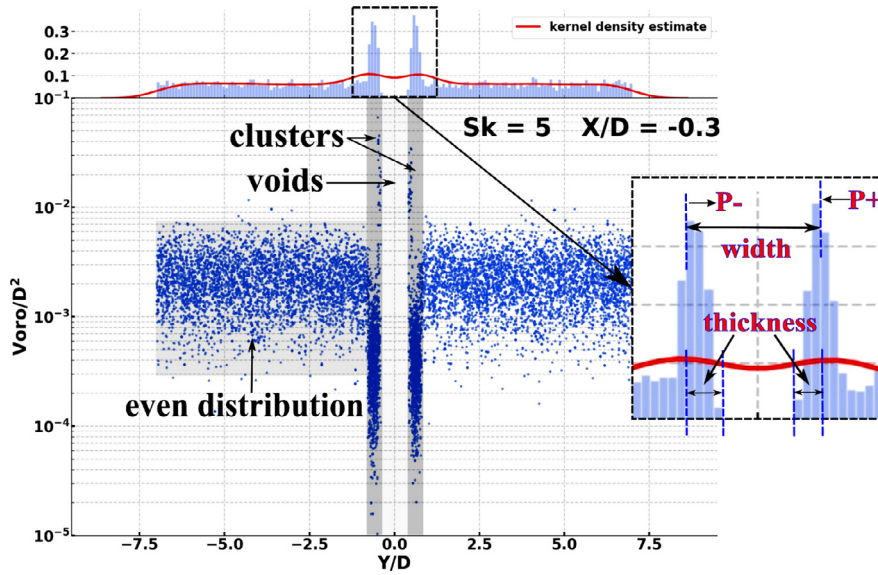
Fig. 3. Illustration of cluster identification at X/D = −0.3 of case Sk = 5. The scatter plot jointly with a histogram and kernel density estimate describe the Voronoï area distribution in the crossflow (Y) direction at both sides of the cylinder. Colored shading regions visualize the clusters (dark gray), voids (light gray) and evenly distributed region (medium gray). P-/+ in the zoom-in plot marks the left/right bin edge corresponding to the outside border of lower/upper bow shock, respectively. The bow shock width and thickness are indicated in the inset. (For interpretation of the references to color in this figure legend, the reader is referred to the web version of this article.)
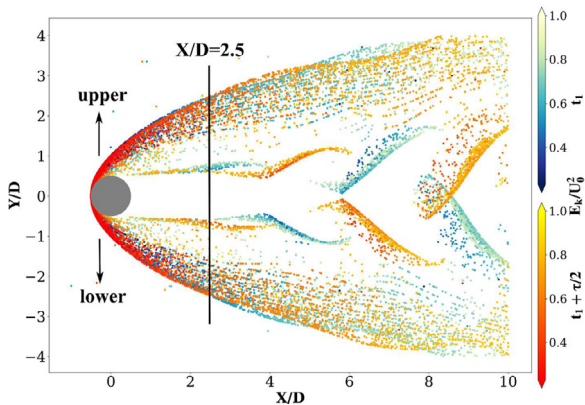
Fig. 4. Instantaneous particle distributions for Sk = 12 at two different time steps t_1 and $t_1 + \tau/2$, where τ is the period of vortex shedding. Particles with velocity magnitude $\leq 0.9U_0$ are not shown. The particles are color-coded according to their normalized kinetic energy. Notice the different color-bars used to distinguish between the two different time steps. The vertical line at X/D = 2.5 indicates the particular location X_c, downstream of which the particle distributions are time dependent. (For interpretation of the references to color in this figure legend, the reader is referred to the web version of this article.)

tion $K(x_i, h)$ is used at its centre to ensure symmetry about this point. The probability density estimation (pdf) is then estimated by adding all of the individual kernel functions corresponding to each sample, and dividing by the number of points. A kernel is controlled by a smoothing parameter known as binwidth, see further and more detailed descriptions of the applied Gaussian KDE in Python. In Fig. 4, we superimpose two particle distribution snapshots, separated in time by half of the shedding period τ. Notice that different colorbars are used for the two different distributions. In the upstream part of the plot, i.e. X/D < 2.5, the two distributions almost perfectly collapse. This demonstrates that the vortex shedding in the wake plays a negligible role on the upstream particle concentration at Stokes number Sk = 12, although the particle concentration downstream of X_c/D = 2.5 is distinctly time dependent. We believe that the particular position X_c, upstream

of which the unsteadiness can be ignored, shifts further downstream with increasing Stokes number. This finding justifies that the particle distributions can be considered as statistically steady and that Voronoï data can be gathered from several different time instants, disregarding the potential need for phase-averaging, in the shedding-unaffected area.

We can define clusters, voids and evenly-distributed regions according to the Voronoï area distribution illustrated in Fig. 3. Of particular interest is the perceptually symmetric clusters where particles accumulate densely within a thin layer at both sides of the cylinder. The left interface (Y/D < 0) corresponds to the outside border of the lower bow shock seen in Fig. 4, while the right interface (Y/D > 0) corresponds to the outside border of the upper bow shock. Fig. 5 presents such Voronoï plots for particles with three different representative Stokes numbers Sk = 5, 16, and 56, one from each of the three different categories in Table 2. We consider two streamwise positions for each Sk, namely X/D = −0.3 and X/D = X_c/D, where the X_c/D is the position upstream of which the particle concentration can be considered to be unaffected by the vortex shedding and therefore time independent. For the three Stokes number shown in Fig. 5, X_c/D $\approx$ 1.1, 2.5 and 5.5, respectively.

It is observed from Fig. 5(a, b, c) that the sharp interfaces on both sides extend further away from the centerline, reflecting that the bow shock widens with downstream distance. In the first row of Fig. 5 for X/D = −0.3, the particles are aggregated densely within a short crossflow range, which is understandable since the outside border is close to the cylinder wall at this upstream position. In comparison with the shapes of the interfaces at downstream positions, shown in the bottom row of Fig. 5, they are less dense and the scatter points become more evenly distributed on both sides of the sharp interface, especially for large Sk. Additionally, the interfaces are getting thinner and shorter downstream, which means that Voronoï cells become larger than the ones upstream of the center of the cylinder. This tendency can also be seen in Fig. 4, namely that the particles are spread away in the cross stream direction and this leads to the less converged distribution downstream. Therefore, it only makes sense to measure the thickness of the bow shock at relatively upstream position due to
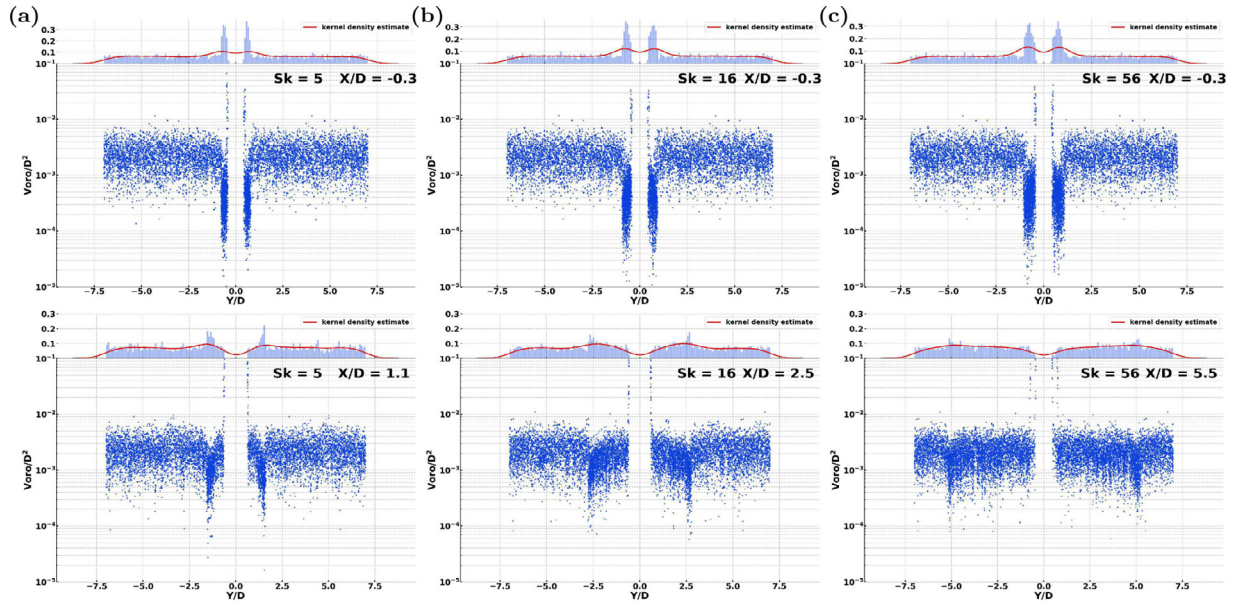
Fig. 5. Voronoï area distributions for three different Stokes numbers are plotted. For each Sk, two downstream positions (X/D) are chosen. (a) Sk = 5, (b) Sk = 16, (c) Sk = 56.

the blurred distributions inside the border of the bow shock in the downstream wake.

In order to quantify the variation of the Voronoï data, we focus on how the *thickness* and *width* of the bow shock change with downstream position and Stokes number. Doing so, we extract the left and right edges of the highest bins on both sides, marked as P−/+, respectively, in Fig. 3. The width W of the bow shock is defined as the distance between P+ and P−. The thickness T is also illustrated in the inset in Fig. 3, which is obtained by subtracting P−/+ and the right/left bin edge of the first non-zero bin on the left/right side. Fig. 6(a) shows how the width of the bow shock varies with increasing downstream positions based on the absolute values of P−/+. This variation is consistent with the observation of the bow shock shape in Fig. 1. We are now in a position to plot the variation of the width W and thickness T as a function of Sk at some downstream positions X/D. The data in Fig. 6(b, c) both show a pronounced increase of the width and thickness for low Sk, while only a modest dependence on Sk is observed for intermediate and high Stokes numbers, particularly so at the downstream position X/D = 0.3.

3.3. Potential flow comparison

In order to explore a possible mechanism for the formation of a bow shock, we examine trajectories of inertial particles in steady potential flow around the circular cylinder. Streamlines of the potential flow are shown in the lower half of Fig. 7(a) and compared with the streamlines of the time-averaged viscous flow field at Re = 100 in the upper half. The two streamline topologies are strikingly different in the wake of the cylinder, as one should expect. Nevertheless, the streamline patterns in the stagnation zone and around the shoulders of the cylinder are rather similar. This close resemblance suggests that the potential flow field can be adopted as a simplified model to explore the behavior of the inertial particles. In this semi-theoretical analysis, the Stokes number is restricted to Sk ≤ 0.14 so that the light particles will not hit the wall, but pass around the cylinder without impacting. A collision model is therefore not required. Ten Sk = 0.1 particles were seeded at the inlet and tracked through the potential flow, without colliding with the cylinder. As the particles approach the cylinder,

their trajectories are deflected upwards in Fig. 7(b) and they tend to converge at about 45°. The convergence of trajectories seem to start near the *inflection point* of the streamlines, from where the inertial spheres gradually depart from the streamlines. Eventually, unlike the streamlines, the particle trajectories gather in a fairly thin layer around the shoulder of the cylinder. The clustered trajectories are only partially following the curvature of the streamlines towards the lee side of the cylinder. A similar pattern of particle trajectories was recently reported by Vallée et al. 2018 for particles moving around a sphere in a potential flow. Also their particles had Stokes number below a certain threshold.

The role played by the inflection point is due to the alteration of the direction of the centrifugal force which tends to make inertial particles move away from the center of curvature. The centrifugal force points in one direction upstream of the inflection point and in the opposite direction downstream of the inflection point. This is believed to have a focusing effect on the trajectories of inertial particles. The centrifuging mechanism will be further explored in Section 4.

Based on an assumption of a low Stokes number, it is possible to derive a first-order approximation for the particle velocity $\boldsymbol{u_p}$ if Sk is taken as a small perturbation parameter. According to Maxey (1987), Goto and Vassilicos, 2008 and Tom and Bragg (2019)

$$\boldsymbol{u_p}(\boldsymbol{x_p}, t) = \boldsymbol{u}(\boldsymbol{x}, t) - Sk\frac{\mathrm{D}\boldsymbol{u}(\boldsymbol{x}, t)}{\mathrm{D}t}\big|_{\boldsymbol{x}=\boldsymbol{x_p}} + O(Sk^2) \tag{6}$$

where $\boldsymbol{x}$ is an arbitrary Euler point in the discretized space covering the particle position $\boldsymbol{x_p}$ and $\mathrm{D}\boldsymbol{u}(\boldsymbol{x}, t)/\mathrm{D}t$ is the fluid acceleration field. By taking the divergence of this simplified particle velocity in Eq. (6), one obtains:

$$\nabla \cdot \boldsymbol{u}_p(\boldsymbol{x_p}, t) = -Sk\nabla \cdot ((\boldsymbol{u}(\boldsymbol{x}, t) \cdot \nabla)\boldsymbol{u}(\boldsymbol{x}, t)|_{\boldsymbol{x}=\boldsymbol{x_p}} \tag{7}$$

Eq. 7 implies that the particle velocity is compressible even if the flow field is incompressible. In particular, the particles are compressed when $\nabla \cdot \boldsymbol{u_p} < 0$.

The divergence of the particle velocity field can now be found from the potential fluid flow field. It turns out that the divergence field shown in Fig. 7(c) only varies with the radial distance from the cylinder surface. The divergence is everywhere large negative and approaches zero at large distances from the cylinder. Large
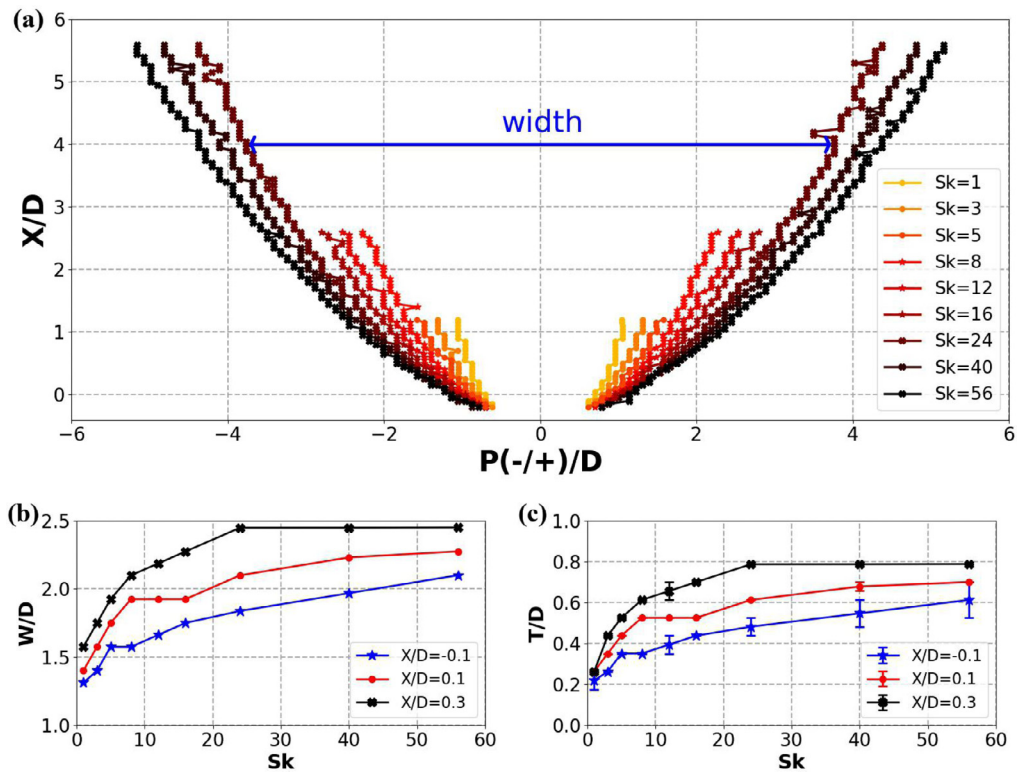
Fig. 6. (a) The location of the bow shock as a function of downstream position X/D for different Stokes numbers (the blue arrow line indicates the bow shock width W). P−/P+ measures the local distance from the symmetry plane (Y = 0). The width W (b) and thickness T (c) vary with Sk. The thickness T in (c) is the average of the bow shock thickness on the two sides of the cylinder. The error bars represent deviations between the two thicknesses. (For interpretation of the references to color in this figure legend, the reader is referred to the web version of this article.)
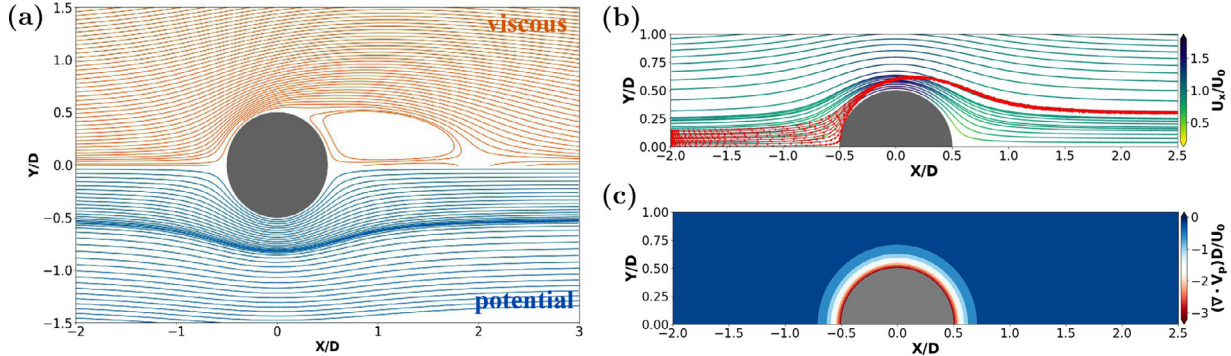

Fig. 7. (a) Comparison of the streamlines between potential flow (blue) and time-averaged viscous flow from numerical simulation (orange). (b) The trajectories of seeded particles with Sk = 0.1 (red dots and lines) in potential flow superimposed with the streamlines. (c) The same trajectories as the ones in (b) superimposed with the first-order approximation of particle divergence in Eq. (7). (For interpretation of the references to color in this figure legend, the reader is referred to the web version of this article.)

negative values are seen in an annular ring around the cylinder. This suggests that the particle field is compressed, i.e. clustered. It is therefore convincing to see that this is the region in which the particle trajectories are converging. The clustering of the trajectories is likely associated with the bow shock formation seen at $Re = 100$.

4. Centrifuging by alternating streamline curvature

The potential flow field and the viscous flow field in Fig. 7(a) are quite similar around the front part of the cylinder (X/D < 0) when it comes to the streamline pattern. A common feature of both is that a streamline with Y/D > 0 first curves upwards and thereafter bends downwards. The center of curvature is first

above the streamline and thereafter below the streamline, which means that the center of curvature switches from above to below at the so-called inflection point (IP) defined mathematically as where the second derivative of the streamline is zero. A fluid element which follows a curved streamline is affected by a force acting in the direction towards the center of curvature. This force is needed to provide the centripetal acceleration towards the center of curvature. In our case, the pressure force is likely to dominate over the viscous force. The pressure force on a fluid element $-dp/dr$, where r for convenience is the radial distance from the center of the cylinder, is first acting outwards until the IP and thereafter inwards. This is indeed plausible since the highest pressure is found in the frontal stagnation point area and a much lower pressure is seen around the shoulders of the cylinder, as shown in Fig. 8(a).
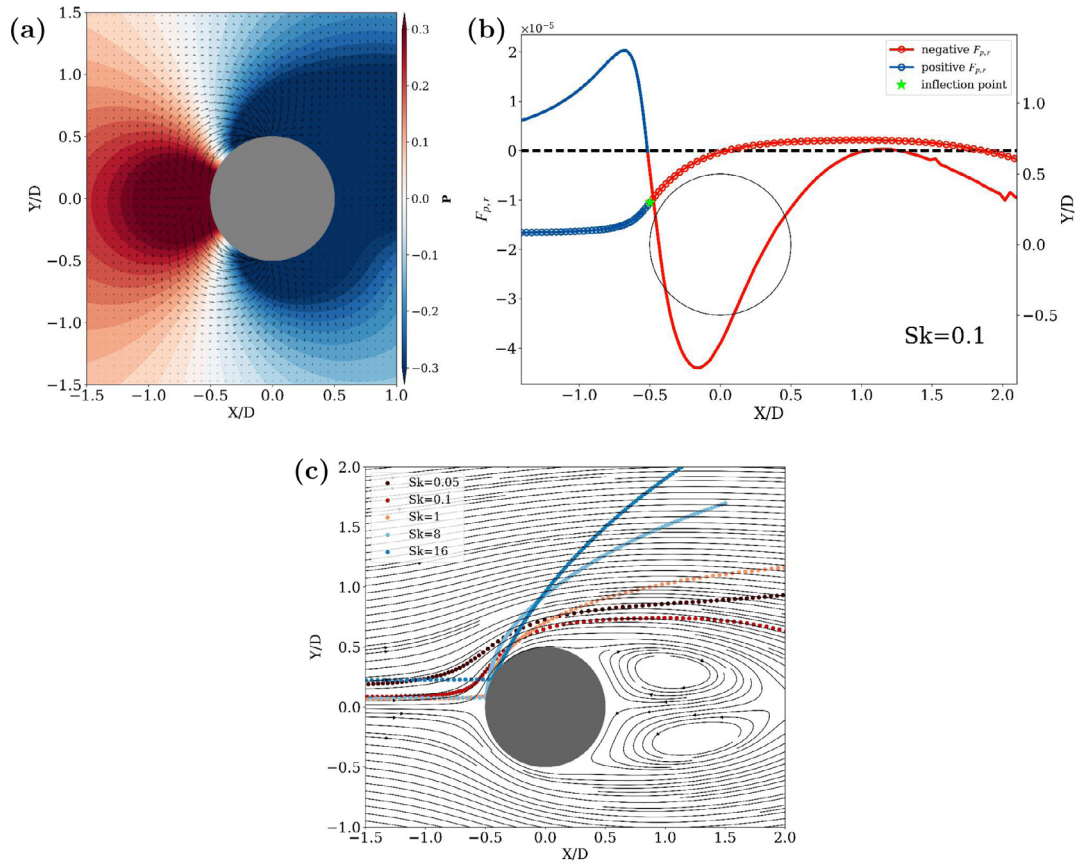
Fig. 8. (a) Pressure distribution (contours) and pressure gradient force (arrows) around the cylinder. (b) Particle trajectory of Sk = 0.1 (line-dot) and the radial component of particle Stokes drag force $F_{r,p}$ (line) at the corresponding position. Blue and orangered colors represent positive and negative $F_{r,p}$, respectively. The inflection point of the particle trajectory is marked with a green star, and well overlapped with the point where $F_{r,p}$ changes the sign along the trajectory. (c) Particle trajectories at Sk = 0.05, 0.1, 1, 8, 16 superimposed with the streamlines of the time-averaged viscous flow. (For interpretation of the references to color in this figure legend, the reader is referred to the web version of this article.)

Analogously, the trajectory of the Sk = 0.1 particle in Fig. 8(b) resembles a streamline. This particle first experiences a positive radial force $F_{p,r}$, which eventually switches to become negative. The switching position, indicated by change of color, is closely related to the IP of the particle trajectory. It should be recalled that the particles are not explicitly affected by the pressure field, but only by the viscous Stokes drag force according to Eq.(3). Along the first stretch of the curved trajectory where the radial force $F_{p,r}$ is positive, the radial fluid velocity is larger than the radial particle velocity. In this region the streamlines divert further away from the circular surface of the cylinder than does the particle trajectory. This situation is reverted when the radial force $F_{p,r}$ changes sign from positive to negative. This happens when the radial particle velocity exceeds the radial fluid velocity and coincides with the IP of the particle trajectory, as indicated in Fig. 8(b).

The centrifugal mechanism is often used to explain why vortical flow structures are depleted of particles. As seen from the curved trajectory of an inertial particle, one usually argues that the real physical radial force (here: the radial component of Stokes drag) is balanced by an oppositely directed fictitious centrifugal force required to make the sum of forces normal to the trajectory equal to zero. In the present case, the centrifugal force inevitably changes sign at the inflection point IP where also the radial drag force changes sign. This physical mechanism is present not only in potential flows but also in viscous flows.

The same arguments apply also for more inertial particles. Trajectories for particles with some different inertia are shown in Fig. 8(c) and superimposed on the time-averaged streamlines at

$Re = 100$. The trajectories of the more inertial particles (Sk ≥ 1) are strongly affected by their impaction on the cylinder surface. After impaction, the trajectory of the Sk = 16 particle is only modestly curved. This is so because the radial component of the Stokes drag is insufficient to balance a substantially larger centrifugal force.

5. Conclusions

In this work, we have conducted three-dimensional numerical simulations of flow around a wetted circular cylinder at $Re = 100$. Particle-fluid (two-way) and particle-particle (four-way) couplings have been neglected in the present study, although these effects may be of some importance in the most densely populated areas, e.g. in the bow shock. We anyhow believe that the novel observations reported herein are qualitatively correct. The unsteady flow was laden with spherical particles whose inertia was parameterized by a Stokes number, Sk. A strong Sk-dependence of the particle distribution was observed both in the vicinity of the cylinder and in the Kámán vortex street. Attention was devoted to the striking and unexpected clustering appearing in front of the cylinder. The width W and thickness T of this particle *bow shock*, which describes how the bow shock developed in the streamwise X-direction, were quantified by means of Voronoï diagrams. At a given streamwise X-location, the width as well as the thickness of the bow shock increased with particle inertia, i.e. with Sk. The further downstream parts of the bow shock are remarkably affected by the periodic shedding at lower Stokes numbers, whereas the

wider bow shock at high Sk is only modestly influenced by the wake dynamics. We also observed that the unexpectedly dense particle accumulation in the upstream part of the shock became more diluted further downstream, most likely as a consequence of the thickening of the bow shock.

To further explore this peculiar phenomenon, we first tracked light particles with Sk = 0.1 in a time-independent potential flow around the cylinder. Such light particles are closely coupled to the carrier fluid and pass around the cylinder. These semi-analytical results do therefore not depend on any collision model. The Lagrangian particle trajectories show a clear tendency to converge at about the same position as the bow shock was formed in the viscous flow simulations. Inspired by the alteration of the direction of the component of the pressure gradient force perpendicular to a curved streamline, we proposed that the change of curvature of the particle trajectories at their inflection point (IP) may enforce a focusing of the trajectories. We therefore tracked a Sk = 0.1 particle through the viscous flow field. The IP of the particle trajectory coincided with the position where the radial component of Stokes drag force changed direction from inwards to outwards, thereby supporting our assumption that the bow shock formation is associated with the focusing of the particle trajectories caused by the centrifugal mechanism.

Acknowledgments

References

Bharadwaj, R., Wassgren, C.R., Zenit, R., 2006. The unsteady drag force on a cylinder immersed in a dilute granular flow. Phys. Fluids 18, 043301. doi:10.1063/1.2191907.

Boudet, J.F., Amarouchene, Y., Kellay, H., 2008. Shock front width and structure in supersonic granular flows. Phys. Rev. Lett. 101, 254503. doi:10.1103/PhysRevLett.101.254503.

Cliff, R., Grace, J., Weber, M.E., 1978. Spheres at higher Reynolds numbers. Bubbles, Drops and Particles. Academic Press, New York, pp. 111–112. Chapter 5

Fessler, J.R., Kulick, J.D., Eaton, J.K., 1994. Preferential concentration of heavy particles in a turbulent channel flow. Phys. Fluids 6, 3742–3749. doi:10.1063/1.868445.

Gobert, C., 2010. Large Eddy Simulation of Particle-Laden Flow. Fakultät für Bauingenieur- und Vermessungswesen PhD dissertation.

Goto, S., Vassilicos, J.C., 2008. Sweep-stick mechanism of heavy particle clustering in fluid turbulence. Phys. Rev. Lett. 100, 054503. doi:10.1103/PhysRevLett.100.054503.

Homann, H., Bec, J., 2015. Concentrations of inertial particles in the turbulent wake of an immobile sphere. Phys. Fluids 27, 053301. doi:10.1063/1.4919723.

Ireland, P.J., Bragg, A.D., Collins, L.R., 2016. The effect of Reynolds number on inertial particle dynamics in isotropic turbulence. Part 1. Simulations without gravitational effects. J. Fluid Mech. 796, 617–658. doi:10.1017/jfm.2016.238.

Joseph, G.G., Zenit, R., Hunt, M.L., Rosenwinkel, A.M., 2001. Particle-wall collisions in a viscous fluid. J. Fluid Mech. 433, 329–346. doi:10.1017/S0022112001003470.

Kantak, A.A., Davis, R.H., 2004. Oblique collisions and rebound of spheres from a wetted surface. J. Fluid Mech. 509, 63–81. doi:10.1017/S0022112004008900.

Kantak, A.A., Davis, R.H., 2006. Elastohydrodynamic theory for wet oblique collisions. Powder Technol. 168, 42–52. doi:10.1016/j.powtec.2006.07.006.

Kim, J., Kim, D., Choi, H., 2001. An immersed-boundary finite-volume method for simulations of flow in complex geometries. J. Comput. Phys. 171, 132–150. doi:10.1006/jcph.2001.6778.

Luo, K., Fan, J., Cen, K., 2009. Transient, three-dimensional simulation of particle dispersion in flows around a circular cylinder Re = 140–260. Fuel 88, 1294–1301. doi:10.1016/j.fuel.2008.12.026.

Manhart, M., 2004. A zonal grid algorithm for DNS of turbulent boundary layers. Comput. Fluids 33, 435–461. doi:10.1016/S0045-7930(03)00061-6.

Manhart, M., Friedrich, R., 2002. DNS of a turbulent boundary layer with separation. Int. J. Heat Fluid Flow 23, 572–581. doi:10.1016/S0142-727X(02)00153-4.

Manhart, M., Tremblay, F., Friedrich, R., 2001. MGLET: a parallel code for efficient DNS and LES of complex geometries. In: Parallel Computational Fluid Dynamics-Trends and Applications. Elsevier Scinece B.V., Amsterdam, pp. 449–456.

Marchioli, C., Soldati, A., 2002. Mechanisms for particle transfer and segregation in a turbulent boundary layer. J. Fluid Mech. 468, 283–315. doi:10.1017/S0022112002001738.

Maxey, M.R., 1987. The gravitational settling of aerosol particles in homogeneous turbulence and random flow fields. J. Fluid Mech. 174, 441–465. doi:10.1017/S0022112087000193.

Maxey, M.R., Riley, J.J., 1983. Equation of motion for a small rigid sphere in a nonuniform flow. Phys. Fluids 26, 883–889. doi:10.1063/1.864230.

Melheim, J.A., 2005. Cluster integration method in Lagrangian particle dynamics. Comput. Phys. Comm. 171, 155–161. doi:10.1016/j.cpc.2005.05.003.

Monchaux, R., Bourgoin, M., 2010. Preferential concentration of heavy particles: A Voronoï analysis. Phys. Fluids 22, 103304. doi:10.1063/1.3489987.

Monchaux, R., Bourgoin, M., Cartellier, A., 2012. Analyzing preferential concentration and clustering of inertial particles in turbulence. Int. J. Multiph. Flow 40, 1–18. doi:10.1016/j.ijmultiphaseflow.2011.12.001.

Nilsen, C., Andersson, H.I., Zhao, L., 2013. A Voronoï analysis of preferential concentration in a vertical channel flow. Phys. Fluids 25, 115108. doi:10.1063/1.4830435.

Peller, N., Duc, A.L., Tremblay, F., Manhart, M., 2006. High-order stable interpolations for immersed boundary methods. Int. J. Numer. Meth. Fluids 52, 1175–1193. doi:10.1002/fld.1227.

Quéré, D., 1999. Fluid coating on a fiber. Annu. Rev. Fluid Mech. 31, 347–384. doi:10.1146/annurev.fluid.31.1.347.

Scriven, L.E., 1988. Physics and applications of dip coating and spin coating. MRS Online Proc. Library Arch. 121, 717–729. doi:10.1557/PROC-121-717.

Shi, W., Anderson, M.J., Tulkoff, J., Kennedy, B.S., Boreyko, J.B., 2018. Flow harvesting with harps. ACS Appl. Mater. Interfaces 10, 11979–11986. doi:10.1021/acsami.7b17488.

Shi, Z., Jiang, F., Andersson, H.I., Strandenes, H., 2019. On simulation of particle-laden wake flow. In: MekIT19 Tenth National Conference on Computational Mechanics. International Center for Numerical Methods in Engineering (CIMNE), pp. 407–418.

Su, S.-W., Lai, M.-C., Lin, C.-A., 2007. An immersed boundary technique for simulating complex flows with rigid boundary. Comput. Fluids 36, 313–324. doi:10.1016/j.compfluid.2005.09.004.

Sumbekova, S., Cartellier, A., Alisede, A., Bourgoin, M., 2017. Preferential concentration of inertial sub-Kolmogorov particles: the roles of mass loading of particles, Stokes numbers, and Reynolds numbers. Phys. Rev. Fluids 2, 024302. doi:10.1103/PhysRevFluids.2.024302.

Tagawa, Y., Mercado, J.M., Prakash, V., Calzavarini, E., Sun, C., Lohse, D., 2012. Three-dimensional Lagrangian Voronoï analysis for clustering of particles and bubbles in turbulence. J. Fluid Mech. 693, 201–215. doi:10.1017/jfm.2011.510.

Tang, L., Wen, F., Yang, Y., Crowe, C.T., Chung, J.N., Troutt, T.R., 1992. Self-organizing particle dispersion mechanism in a plane wake. Phys. Fluids 4, 2244–2251. doi:10.1063/1.858465.

Tom, J., Bragg, A.D., 2019. Multiscale preferential sweeping of particles settling in turbulence. J. Fluid Mech. 871, 244–270. doi:10.1017/jfm.2019.337.

Tseng, Y.-H., Ferziger, J.H., 2003. A ghost-cell immersed boundary method for flow in complex geometry. J. Comput. Phys. 192, 593–623. doi:10.1016/j.jcp.2003.07.024.

Uhlmann, M., 2008. Interface-resolved direct numerical simulation of vertical particulate channel flow in the turbulent regime. Phys. Fluids 20, 053305. doi:10.1063/1.2912459.

Vallée, R., Henry, C., Hachem, E., Bec, J., 2018. Inelastic accretion of inertial particles by a towed sphere. Phys. Rev. Fluids 3, 024303. doi:10.1103/PhysRevFluids.3.024303.

Wassgren, C.R., Cordova, J.A., Zenit, R., Karion, A., 2003. Dilute granular flow around an immersed cylinder. Phys. Fluids 15, 3318–3330. doi:10.1063/1.1608937.

Williamson, C.H.K., 1996. Vortex dynamics in the cylinder wake. Annu. Rev. Fluid Mech. 28, 477–539. doi:10.1146/annurev.fl.28.010196.002401.

Wood, A.M., Hwang, W., Eaton, J.K., 2005. Preferential concentration of particles in homogeneous and isotropic turbulence. Int. J. Multiph. Flow 31, 1220–1230. doi:10.1016/j.ijmultiphaseflow.2005.07.001.

Yang, Y., Crowe, C.T., Chung, J.N., Troutt, T.R., 2000. Experiments on particle dispersion in a plane wake. Int. J. Multiph.. Flow 26, 1583–1607. doi:10.1016/S0301-9322(99)00105-6.

Zdravkovich, M.M., 1997. Flow Around Circular Cylinders. Volume I: Fundamentals. Oxford University Press, Oxford.

Zhao, L., Andersson, H.I., Gillissen, J.J.J., 2010. Turbulence modulation and drag reduction by spherical particles. Phys. Fluids 22, 081702. doi:10.1063/1.3478308.

Zhou, H., Mo, G., Cen, K., 2011. Numerical investigation of dispersed gas-solid two-phase flow around a circular cylinder using lattice Boltzmann method. Comput. Fluids 52, 130–138. doi:10.1016/j.compfluid.2011.09.007.